RSC Advances

PAPER

View Article Online
View Journal | View Issue



Cite this: *RSC Adv.*, 2026, **16**, 12215

# Balancing high performance with synthesis complexity: one-step hydrothermal growth of self-supported $NiCo_2Se_4$ nanoflowers on carbon cloth for advanced asymmetric supercapacitors

Junyu Guo,[a] Yawei Hu,*[ab] Jiasheng Li,[a] Xuzhao Peng[a] and Jianbo Tong*[ab]

Received 4th January 2026
Accepted 6th February 2026

DOI: 10.1039/d6ra00083e

rsc.li/rsc-advances

Bimetallic transition-metal selenides are promising supercapacitor electrodes due to their high theoretical capacitance and rich redox activity. However, achieving high performance often relies on complex multi-step syntheses, limiting practical application. Herein, a simplified one-step hydrothermal strategy is employed to directly grow hierarchical $NiCo_2Se_4$ nanoflowers on flexible carbon cloth (CC). This *in situ* strategy eliminates binders and conductive additives, reduces interfacial resistance, and enhances structural integrity. The optimized $NiCo_2Se_4$/CC electrode delivers a competitive specific capacitance of 1479 F $g^{-1}$ (4.42 F $cm^{-2}$)at 1 A $g^{-1}$, excellent rate capability (90.1% retention at 10 A $g^{-1}$), and stable cycling performance (84% retention after 5000 cycles). An asymmetric supercapacitor assembled with activated carbon achieves 30.39 Wh $kg^{-1}$ at 2549.9 W $kg^{-1}$ and maintains 87.6% capacitance after 20 000 cycles. Overall, this work shows that competitive electrochemical performance can be achieved through a streamlined one-step synthesis, offering a practical and scalable fabrication route without complex post-processing.

## 1 Introduction

The accelerating demand for advanced energy-storage technologies has intensified the search for highly efficient electrode materials.[1–3] Supercapacitors (SCs), with their fast charge–discharge kinetics and excellent cycling stability, are considered promising candidates for next-generation energy systems.[4–7] However, their relatively low energy density remains a major bottleneck.[8] Considerable efforts have therefore focused on transition-metal-based oxides, sulfides, and selenides, where selenium-based materials have attracted increasing attention due to their favorable electronic structure, tunable redox chemistry, and strong interaction with conductive substrates, as comprehensively reviewed in recent literature. However, in many reported systems, performance enhancement is often achieved at the expense of synthetic simplicity, raising concerns regarding scalability and practical implementation.[9–13]

Recent studies further suggest that multi-step hydrothermal, vulcanization, or composite-engineering strategies—although designed to refine morphology or improve conductivity—improved performance.[14] In this context, $NiCo_2Se_4$ and related Ni–Co bimetallic selenide systems have attracted considerable attention as representative pseudocapacitive materials owing to their relatively high intrinsic conductivity and rich redox activity, and have been widely investigated as model electrode systems for supercapacitors, particularly in carbon-supported architectures.[15]

In recent years, morphological modulation and structural engineering of $NiCo_2Se_4$ have emerged as effective strategies for enhancing its charge-storage capability. For instance, Li *et al.* constructed morphology-tunable $NiCo_2Se_4$ nanoarrays on carbon cloth through a two-step hydrothermal-selenization route, achieving a specific capacitance of 1100–1300 F $g^{-1}$.[16] Meanwhile, Ghosh *et al.* synthesized $NiCo_2Se_4$/RGO composites *via* a one-step hydrothermal method and optimized the crystallinity and conductive pathways by varying the reaction duration, delivering 900–1200 F $g^{-1}$.[17] Zhang *et al.* fabricated mesoporous $NiCo_2Se_4$ nanotubes using a template-assisted two-step approach; their hierarchical porous structure facilitated rapid ion diffusion, enabling capacitances of~1000–1400 F $g^{-1}$ at 1 A $g^{-1}$.[18] In addition, Chen *et al.* employed a three-step strategy—Ni/C pretreatment, precursor growth, and time-dependent selenization—to obtain hollow nanotube arrays, which exhibited a high charge-storage capacity of 306.4 mAh $g^{-1}$ (≈1379 F $g^{-1}$).[19] Furthermore, Wang *et al.* prepared uniform bimetallic $NiCo_2Se_4$ particles through a one-step hydrothermal process, achieving an equivalent capacitance of 700–1100 F $g^{-1}$.[20] These values fall within a broadly comparable performance range. Although these studies demonstrate that

[a]*College of Chemistry and Chemical Engineering, Shaanxi University of Science and Technology, Xi'an 710021, China*

[b]*Shaanxi Key Laboratory of Chemical Additives for Industry, Xi'an 710021, China. E-mail: huyawei@sust.edu.cn; jianbotong@aliyun.com*

$NiCo_2Se_4$ can deliver high gravimetric capacitance, achieving such performance is commonly achieved through multistep synthesis, prolonged reaction times, template assistance, or controlled-atmosphere selenization.[21] Directly growing active materials on conductive substrates represents a viable alternative by eliminating binders and improving charge-transfer efficiency, and extensive studies have highlighted how carbon nanostructure design, interfacial contact engineering, and optimized metal/semiconductor–carbon interfaces can significantly enhance electron transport and redox accessibility in pseudocapacitive systems.[22–25] Carbon cloth (CC), with its interconnected 3D conductive network and excellent mechanical flexibility, has emerged as an ideal scaffold.[26–30] However, many reported $NiCo_2Se_4$/CC electrodes still involve multistep precursor conversion or post-selenization treatments, which introduces additional complexity and partially offsets the advantages of the CC scaffold.[31–33]

In this work, we explore how precursor chemistry, bimetallic co-nucleation behavior, and substrate confinement can be coordinated within a one-step hydrothermal process to explore the electrochemical performance achievable under a simplified synthesis route. Using this one-step hydrothermal approach, hierarchical $NiCo_2Se_4$ nanoflower structures are formed *in situ* on flexible carbon cloth, whereby material synthesis, morphological construction, and electrode integration are accomplished simultaneously without the use of binders, conductive additives, or any post-treatment steps.[34–36] Through deliberate precursor design and controlled nucleation kinetics, the resulting $NiCo_2Se_4$/CC electrode features (i) a 3D porous nanoflower architecture that facilitates rapid ion transport,[37] (ii) mixed Ni/Co valence states that enhance redox activity,[38] and (iii) strong interfacial bonding that likely contributes to reduced charge-transfer resistance.[39] These results suggest that morphology control, electronic optimization, and direct substrate integration can be effectively coordinated within a single-step route, providing a reasonable balance between electrochemical performance and synthetic simplicity. Under these conditions, the electrode delivers a specific capacitance of 1479 F $g^{-1}$ at 1 A $g^{-1}$, together with good rate capability and stable long-term cycling performance.[40–43] When paired with activated carbon, the resulting asymmetric supercapacitor achieves competitive energy and power densities along with good cycling stability.[44–47] Overall, this work demonstrates that electrochemical performance comparable to previously reported $NiCo_2Se_4$-based electrodes can be achieved using a streamlined one-step fabrication strategy, provided that precursor chemistry, bimetallic interactions, and substrate effects are appropriately coordinated. This study does not aim to introduce a new material system, but rather offers insight into how practical electrode architectures can be realized without relying on elaborately engineered multistep syntheses.[48–51]

# 2 Experimental

## 2.1. Design philosophy: reconciling performance with process simplicity

Developing high-performance electrodes for supercapacitors has traditionally relied on a fragmented, multi-step fabrication route involving the synthesis of active materials, incorporation of conductive additives and polymeric binders, slurry formulation, coating onto metallic current collectors, and subsequent drying and pressing. Although widely adopted, this workflow inherently increases processing time, energy demand, and manufacturing cost. More importantly, each step can introduce interfacial discontinuities—particularly between the active material, binders, and current collector—that impede electron/ion transport and limit the effective utilization of electroactive sites.

Our design philosophy seeks to fundamentally reconfigure this paradigm through integration rather than accumulation. Instead of treating synthesis, morphology control, and electrode construction as discrete stages, we consolidate them into a single hydrothermal step. This integrated strategy simultaneously directs the nucleation and growth of hierarchical $NiCo_2Se_4$ nanostructures and anchors them directly onto the 3D conductive framework of carbon cloth. By removing binders, conductive additives, and post-synthetic treatments, the approach minimizes artificial interfaces, strengthens electronic coupling at the $NiCo_2Se_4$/CC junction, and promotes efficient charge-transfer pathways.

As summarized in the revised Table S3, previously reported $NiCo_2Se_4$-based electrodes span a wide range of electrochemical performance and synthesis complexity. While multistep or template-assisted strategies often achieve high capacitance, they typically involve post-thermal treatment, atmosphere control, or prolonged processing. In contrast, one-step routes generally offer reduced complexity but more moderate performance. Our approach falls within this simplified category, while achieving capacitance values comparable to the upper range of reported results.

## 2.2. Facile one-step fabrication of self-supported $NiCo_2Se_4$/CC electrodes

$NiCo_2Se_4$ nanostructures were grown directly on carbon cloth through a facile one-step hydrothermal method. A homogeneous precursor solution containing $Ni^{2+}$, $Co^{2+}$, selenium, urea, and hydrazine hydrate was prepared and used as the reaction medium. The pretreated carbon cloth was immersed in the solution and subjected to hydrothermal treatment at 180 °C for 12 h. After washing and drying, the resulting product was denoted as $NiCo_2Se_4$/CC and used directly as a binder-free working electrode.

For comparison, $NiSe_2$/CC and $CoSe_2$/CC were synthesized under identical hydrothermal conditions by replacing the bimetallic precursor with the respective monometallic salt. All detailed synthetic procedures, reagent quantities, and mass-loading measurements are provided in the SI.

## 2.3. Material characterization

All characterizations were carried out directly on the as-prepared self-supported electrodes to ensure that the observed structural and compositional features accurately reflect their operational state during electrochemical testing. The surface morphology and microstructural features were examined using

scanning electron microscopy (SEM, ZEISS Sigma 300) operated at 5 kV. Transmission electron microscopy (TEM), high-resolution TEM (HRTEM), and energy-dispersive X-ray spectroscopy (EDS) elemental mapping were performed using an FEI Talos 200X microscope at 200 kV. For TEM characterization, the $NiCo_2Se_4$ material was gently detached from the carbon cloth, ultrasonically dispersed in ethanol, and drop-cast onto a copper grid. This additional preparation step was required due to the 3D interconnected nature of the carbon cloth, which prevents direct TEM observation.X-ray diffraction (XRD) patterns were collected on a Bruker D8 Advance diffractometer using Cu Kα radiation ($\lambda$ = 1.5418 Å) over a $2\theta$ range of 10–80°. X-ray photoelectron spectroscopy (XPS) was conducted on a Thermo Scientific K-Alpha system equipped with Al Kα radiation, and all binding energies were calibrated to the C 1s reference peak at 284.8 eV. These structural and chemical analyses were employed to verify phase purity, oxidation states, and elemental distribution in the $NiCo_2Se_4$/CC electrodes prepared by the one-step synthesis.

### 2.4. Electrochemical evaluation

**2.4.1. Electrochemical evaluation consists of two parts.** Intrinsic characterization using a three-electrode system and practical device testing using a two-electrode asymmetric supercapacitor (ASC) configuration.

**2.4.2. Three-electrode measurements.** All electrochemical measurements were conducted at room temperature using a CHI660E electrochemical workstation (Shanghai Chenhua). The self-supported $NiCo_2Se_4$/CC electrode (1 × 1 $cm^2$, single-side active area ≈ 1 $cm^2$) was used as the working electrode, with a platinum foil and a saturated calomel electrode (SCE) serving as the counter and reference electrodes, respectively. All tests were performed in 2 M KOH aqueous electrolyte. Cyclic voltammetry (CV) was conducted from 0 to 0.6 V (*vs.* SCE) at scan rates of 1–50 mV $s^{-1}$. Galvanostatic charge–discharge (GCD) measurements were carried out between 0 and 0.5 V. For electrochemical measurements, cyclic voltammetry (CV) was performed over a slightly wider potential window to clearly identify redox features and capacitive behavior, while galvanostatic charge–discharge (GCD) tests were conducted within a relatively narrower and electrochemically stable potential range to ensure linear charge–discharge profiles and avoid polarization effects at the voltage limits. All electrochemical parameters reported in this work were extracted from GCD curves measured within the stable potential window. Electrochemical impedance spectroscopy (EIS) was recorded at open-circuit potential over a frequency range from 0.01 Hz to 100 kHz with an amplitude of 5 mV.

**2.4.3. Fabrication and testing of the asymmetric supercapacitor (ASC).** To assess practical applicability, an ASC device was assembled using $NiCo_2Se_4$/CC as the positive electrode and activated carbon (AC) coated on carbon cloth as the negative electrode. The AC electrode was prepared by mixing AC, carbon black, and polyvinylidene fluoride (PVDF) binder in a mass ratio of 7 : 2 : 1 in *N*-methyl-2-pyrrolidone (NMP) to form a homogeneous slurry. This ratio is widely adopted for AC-based electrodes to ensure good conductivity and mechanical stability. The slurry was coated onto carbon cloth (1 × 2 $cm^2$) and dried at 80 °C for 12 h.

The mass loading of the AC electrode was adjusted based on the charge-balance equation:

$$m^+ C^+ \Delta V^+ = m^- C^- \Delta V^- \quad (1)$$

Ensuring equal charge storage between the two electrodes. The electrodes were separated by a cellulose membrane and assembled in a flexible two-electrode sandwich configuration with 2 M KOH as the electrolyte. The operating voltage window of the ASC was determined from preliminary CV scans.

The energy and power densities of the ASC were calculated based on the total mass of both the positive $NiCo_2Se_4$/CC electrode and the negative activated carbon electrode. Capacitance and Energy/Power Density Calculations:

The specific capacitance ($C$) of the electrode was calculated using the following equation:

$$C = \frac{I \times \Delta t}{m \times \Delta V} \quad (2)$$

where $I$ (A) is the discharge current, $\Delta t$ (s) is the discharge time, $m$ (g) is the mass of active material, and $\Delta V$ (V) is the potential window during discharge. Here, $m$ refers exclusively to the mass of electroactive $NiCo_2Se_4$, excluding the mass of the carbon cloth substrate.

The energy density ($E$) and power density ($P$) of the ASC device were calculated as follows:

$$E = \frac{CV^2}{2 \times 3600} \quad (3)$$

$$P = \frac{3600 \times E}{\Delta t} \quad (4)$$

Here, $C$ (F $g^{-1}$) denotes the specific capacitance of the full ASC device, obtained from its GCD curves, $V$(v) is the operating voltage window, and $\Delta t$ (s) is the discharge time.

All electrochemical measurements were conducted on at least three independently prepared electrodes (and devices) to ensure reproducibility, and consistent trends were observed across different samples.

## 3 Results and discussion

### 3.1. The specific procedure for the one-step *in situ* growth of $NiCo_2Se_4$ on carbon cloth ($NiCo_2Se_4$/CC)

Fig. 1 schematic illustration of the *in situ* growth of $NiCo_2Se_4$ on carbon cloth. $NiCo_2Se_4$/CC was synthesized *via* a one-step hydrothermal method. Specifically, appropriate amounts of Ni and Co salts together with a selenium source were dissolved in deionized water to form a homogeneous precursor solution. The pre-treated carbon cloth was immersed in the solution and transferred into a Teflon-lined autoclave, followed by hydrothermal reaction at 180 °C for 12 h. After cooling to room temperature, the obtained $NiCo_2Se_4$/CC electrode was washed and dried for further use.

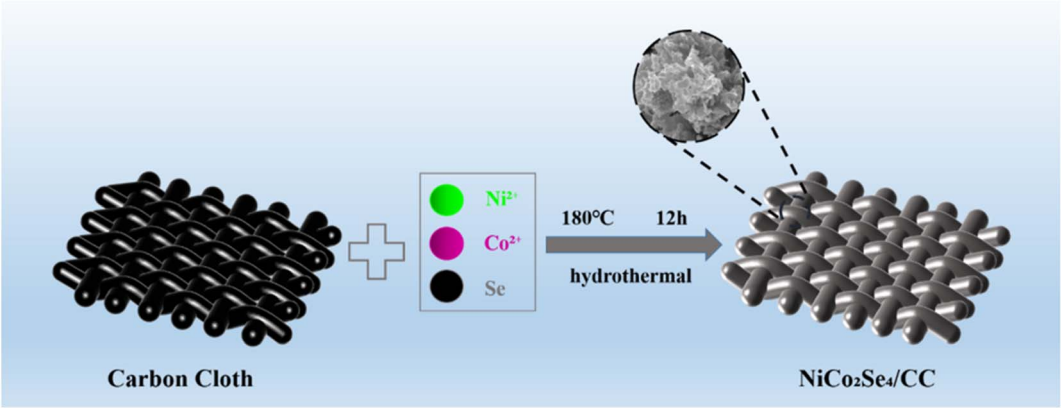


Fig. 1 Schematic synthesis process to $NiCo_2Se_4$/CC composite.

### 3.2. Structural and morphological advantages of the one-step *in situ* grown $NiCo_2Se_4$/CC

For a fair comparison, the control electrodes ($NiSe_2$/CC and $CoSe_2$/CC) were synthesized under identical hydrothermal conditions, and their mass loadings were carefully controlled to be comparable to that of $NiCo_2Se_4$/CC ($\approx 3 \pm 0.2$ mg cm$^{-2}$).

The pronounced morphological divergence between monometallic and bimetallic selenides reveals the fundamental advantage of the one-step *in situ* hydrothermal growth strategy. As shown in Fig. 2, $NiSe_2$/CC (Fig. 2b) develops compact block-like aggregates, while $CoSe_2$/CC (Fig. 2c) forms interlaced rod bundles with limited porosity. Under otherwise identical reaction conditions, introducing both $Ni^{2+}$ and $Co^{2+}$ precursors dramatically shifts the crystallization pathway, yielding a hierarchical nanosheet morphology constructed from ultrathin, interconnected nanosheets (Fig. 2a). Synergistic bimetallic nucleation may influence the nanosheet-dominated growth.$Ni^{2+}$ and $Co^{2+}$ possess distinct hydrolysis kinetics and coordination preferences toward selenide species. When co-existing in solution, their simultaneous hydrolysis increases

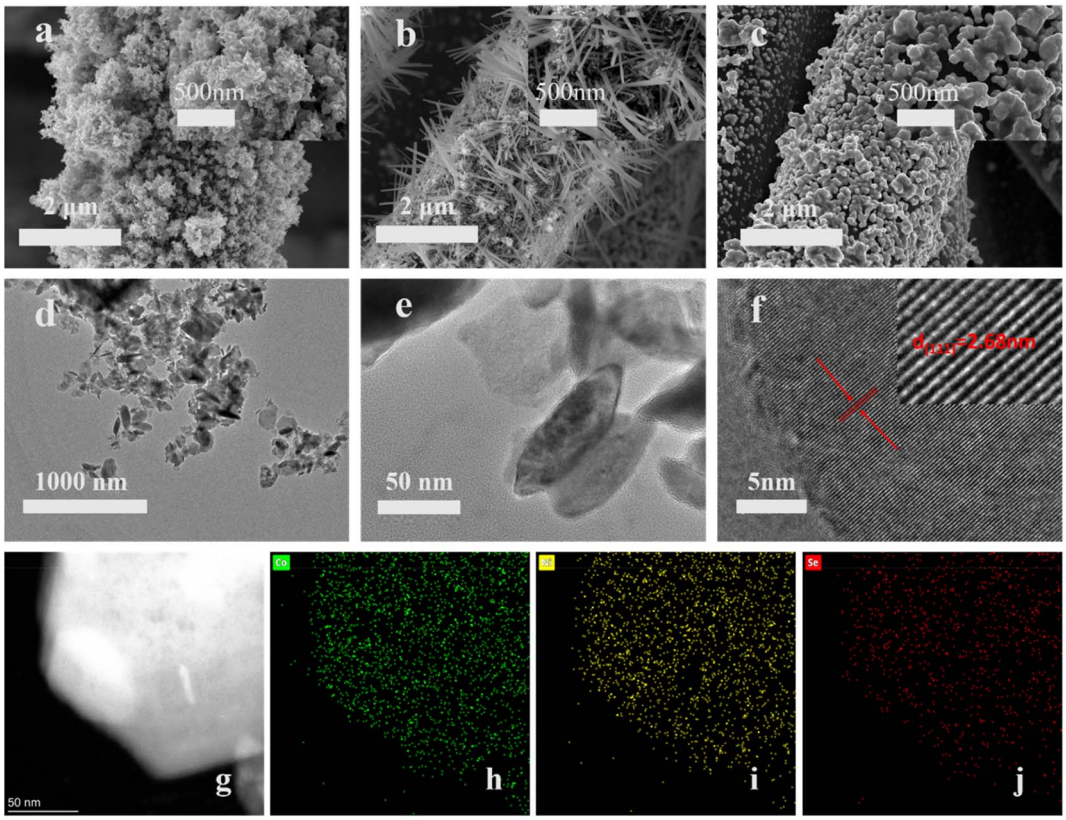


Fig. 2 SEM images of (a) $NiCo_2Se_4$/CC, (b) $CoSe_2$/CC, (c) $NiSe_2$/CC and TEM image of (d). (e) $NiCo_2Se_4$/CC and (f) HRTEM image of $NiCo_2Se_4$/CC and (g–j) elemental mappings of Ni, Co and Se elements.

the density of initial nuclei while altering the local coordination environment, suppressing the anisotropic facet growth that dominates monometallic systems. Instead, co-nucleation at multiple sites restricts directional crystal extension and thermodynamically favors two-dimensional sheet formation. This "mutual growth suppression" between Ni-rich and Co-rich nuclei may favors nanosheet-dominated growth into a nanosheet-dominated regime, explaining why the bimetallic system cannot evolve into the block-like or rod-shaped morphologies observed in the single-metal analogues. The carbon cloth substrate further directs nanosheet anchoring and hierarchical self-assembly. Owing to its abundant defect sites and oxygen-containing functional groups, carbon cloth (CC) provides a chemically active surface that facilitates heterogeneous nucleation and intimate interfacial binding. The highly conductive CC fibers serve simultaneously as (i) an electron-conducting backbone and (ii) a 3D geometric scaffold that restricts lateral sheet ripening, with the observed morphology suggesting effective electron transport and structural guidance. This geometrical confinement may promote vertical sheet anchoring, allowing the 2D nanosheets to assemble radially into hierarchical nanoflowers instead of forming random agglomerates. Such substrate–material coupling is a potential benefit of *in situ* grown self-supported electrodes compared with powder-based ones. Although the three electrodes possess comparable mass loading and substrate coverage, their distinct morphologies result in markedly different electrochemical behaviors. The hierarchical nanosheet architecture of $NiCo_2Se_4$ provides more accessible active sites and shorter ion-diffusion pathways than the block-like $NiSe_2$ or rod-like $CoSe_2$ structures, thereby leading to superior rate capability and capacitance. It should be noted that this mechanistic interpretation is derived from comparative structural observations under identical synthesis conditions, rather than from time-resolved or *in situ* characterization, and therefore represents a plausible but not definitive growth pathway.

TEM analyses are consistent with the proposed crystallization mechanism. Low-magnification TEM (Fig. 2d) confirms the presence of the nanosheet-assembled hierarchical motif predicted by the multi-site nucleation model, while HRTEM (Fig. 2f) shows well-defined lattice fringes with a spacing of 0.268 nm corresponding to the (111) plane of spinel $NiCo_2Se_4$. Slight lattice distortions and partially disordered regions are observed, which are often observed in rapidly grown bimetallic selenides and indicate the presence of structural defects that may influence surface properties. Elemental mapping (Fig. 2g–j) confirms homogeneous distribution of Ni, Co, and Se across the nanosheets, validating the formation of a single-phase bimetallic framework and excluding phase separation into $NiSe_2$/$CoSe_2$ domains. This seamless elemental mixing supports the proposed cooperative nucleation mechanism. This structure–function coupling provides a plausible explanation for the superior electrochemical response.

The resulting $NiCo_2Se_4$/CC nanoflower architecture integrates three structural advantages: (i) ultrathin nanosheets provide abundant accessible redox-active sites; (ii) open hierarchical porosity reduces ion diffusion resistance; (iii) direct growth on a conductive CC network ensures rapid and continuous electron transport.

Together, these features establish a highly efficient ion–electron transport matrix, explaining the substantially enhanced pseudocapacitive behavior relative to the block-like $NiSe_2$ and rod-like $CoSe_2$ counterparts.

### 3.3. Crystallographic and chemical state analysis

The crystallographic structure of the $NiCo_2Se_4$/CC electrode was examined by XRD (Fig. 3). The diffraction pattern displays distinct reflections at 29.9°, 33.5°, 36.9°, 51.8°, and 54.7°, which correspond to the (200), (210), (211), (311), and (230) planes of cubic spinel $NiCo_2Se_4$ (PDF#97-062-4485). The absence of additional crystalline phases indicates that the one-step hydrothermal process successfully yields phase-pure $NiCo_2Se_4$ directly on the carbon cloth substrate. Although XRD cannot rule out trace amorphous species, no detectable signatures of monometallic $NiSe_2$ or $CoSe_2$ are observed in the main pattern.

For comparison, the XRD patterns of $NiSe_2$/CC and $CoSe_2$/CC are provided in the SI (Fig. S1). Their respective diffraction peaks match well with the standard cards for orthorhombic $NiSe_2$ (PDF#97-064-6527) and cubic $CoSe_2$ (PDF#97-062-4998), confirming that the phase outcome is precisely dictated by the precursor composition. This comparison highlights a compositional-controlled phase evolution: the coexistence of $Ni^{2+}$ and $Co^{2+}$ favors the stabilization of the ternary spinel $NiCo_2Se_4$ rather than the formation of monometallic selenides.

The broad features near 26° and 43° originate from the turbostratic (002) and in-plane (100)/(101) carbons of the carbon cloth. Notably, the diffraction peaks of $NiCo_2Se_4$/CC are visibly broader than those of the monometallic analogues in Fig. S1, suggesting smaller coherent crystallite domains and enhanced lattice distortion. Such peak broadening is characteristic of rapid *in situ* nucleation on conductive fiber substrates and the random distribution of dual-metal cations within the spinel lattice. These structural characteristics are advantageous for electrochemical storage, as reduced crystallite sizes and defect-

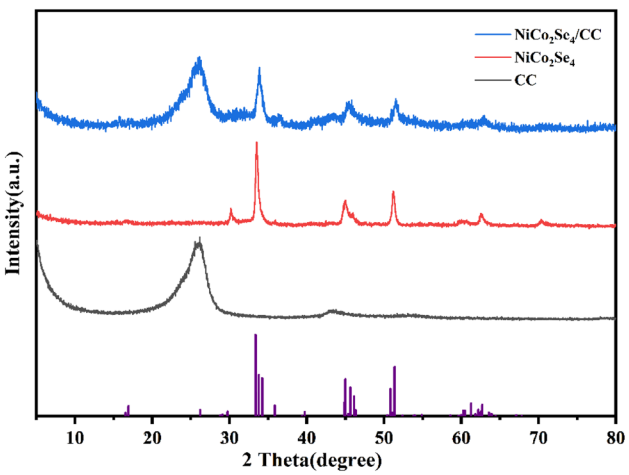


Fig. 3 XRD pattern of CC, $NiCo_2Se_4$ and $NiCo_2Se_4$/CC composites.

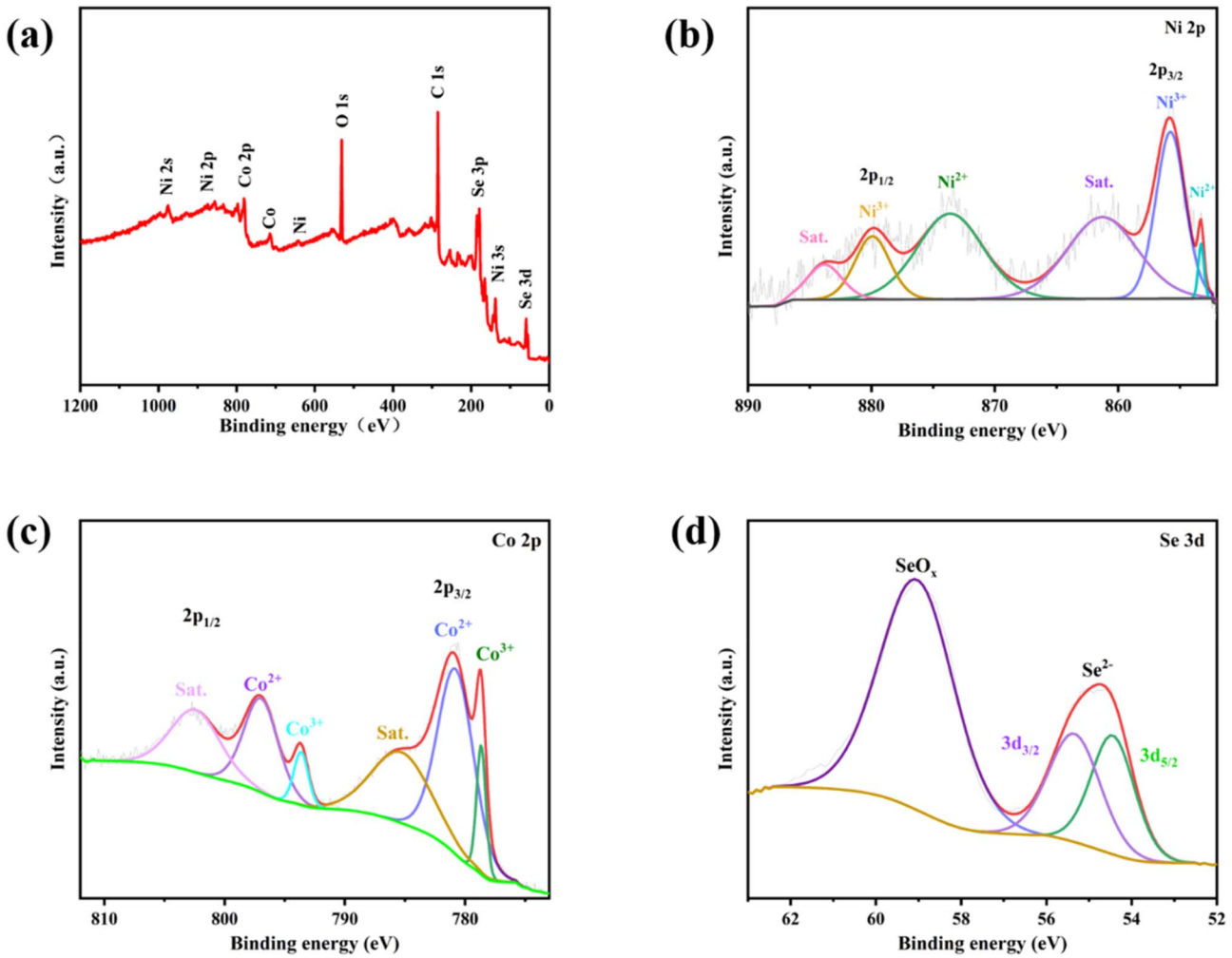


Fig. 4 (a) XPS survey spectrum, (b) Ni 2p, (c) Co 2p and (d) Se 3d high resolution XPS spectra of $NiCo_2Se_4$/CC.

rich lattices expose more electrochemically accessible active sites and facilitate faster ion diffusion.

Overall, the XRD results verify the successful formation of phase-pure spinel $NiCo_2Se_4$ on carbon cloth and reveal its inherently nano-crystalline and defect-enriched nature, consistent with the hierarchical nanosheet morphology described earlier and beneficial for the subsequent electrochemical performance.

XPS analysis (Fig. 4) provides direct evidence of the surface-valence configuration and electronic-structure modulation induced by bimetallic incorporation.

In the Ni 2p spectrum (Fig. 4b), two main peaks located at ~855.6 eV (Ni $2p_{3/2}$) and ~873.1 eV (Ni $2p_{1/2}$), together with their corresponding satellite peaks at ~861.2 and ~879.1 eV, are characteristic of $Ni^{2+}$ in selenide frameworks. A shoulder on the high-binding-energy side of the Ni $2p_{3/2}$ peak indicates the presence of a minor $Ni^{3+}$ component, which may originate from surface oxidation and the non-stoichiometric coordination environment may arise from conditions during hydrothermal selenization.

Similarly, the Co 2p spectrum (Fig. 4c) displays well-defined $Co^{2+}$ peaks at ~780.4 eV ($2p_{3/2}$) and ~796.0 eV ($2p_{1/2}$) with minor satellite structures, while the subtle peak shift and shoulder features reveal a partial contribution of $Co^{3+}$. The coexistence of dual oxidation states for both Ni and Co confirms that the bimetallic $NiCo_2Se_4$ lattice accommodates valence-flexible cations, a hallmark of spinel-type redox centers that can undergo fast $M^{2+}/M^{3+}$ transitions during charge storage.

The Se 3d spectrum (Fig. 4d) shows a dominant doublet at ~54.4/55.3 eV, assigned to $Se^{2-}$-in metal selenides, accompanied by a weak component near ~59.0 eV from surface $SeO_x$ species. The presence of $SeO_x$ is consistent with surface reconstruction due to lattice strain, as confirmed by HRTEM-observed fringe distortion and locally amorphous regions. Such $SeO_x$-terminated surfaces are known to enhance wettability and promote interfacial charge-transfer kinetics.

Quantitative peak deconvolution was performed on the high-resolution Ni 2p and Co 2p XPS spectra to estimate the relative fractions of different oxidation states (Table S2).For Ni, the fitted $Ni^{2+}$ and $Ni^{3+}$ components account for approximately 27.22% and 36.40%, respectively, indicating a mixed-valence configuration.Similarly, the Co 2p spectrum reveals coexistence of $Co^{2+}$ (57.62%) and $Co^{3+}$ (13.51%) species.The presence of mixed Ni and Co valence states is generally considered

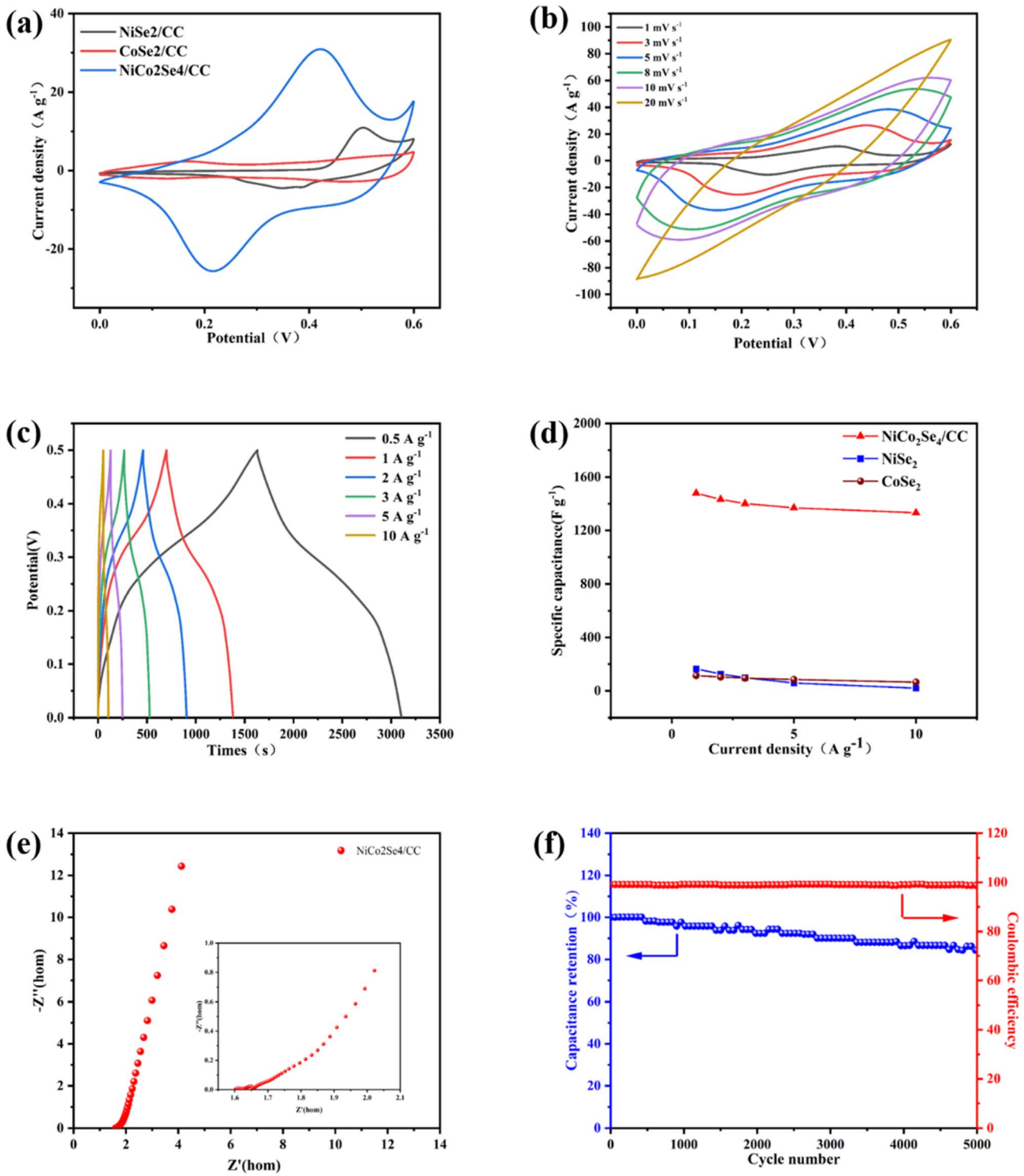


Fig. 5 (a) CV curves at a scanning rate of 10 mV $s^{-1}$ for $NiSe_2$/CC, $CoSe_2$/CC, and $NiCo_2Se_4$/CC electrodes. (b) CV curves at varied scan rate for $NiCo_2Se_4$/CC electrodes. (c) GCD curves at varied current densities for the $NiCo_2Se_4$/CC electrodes. (d) The specific capacitance of $NiSe_2$/CC, $CoSe_2$/CC, and $NiCo_2Se_4$/CC electrodes. (e) Nyquist plots of $NiCo_2Se_4$/CC (f) cycling performance of $NiCo_2Se_4$/CC electrodes at 15 A $g^{-1}$.

favorable for facilitating reversible redox reactions and enhancing pseudocapacitive charge storage.

Importantly, the simultaneous presence of $Ni^{2+}/Ni^{3+}$ and $Co^{2+}/Co^{3+}$, coupled with uniform elemental distribution (Fig. 2g–j), indicates strong bimetallic electronic coupling within the Ni–Co–Se framework. The hybridization of Ni-3d and Co-3d orbitals modulates the local electronic density around the Se sites and likely contributes to reduced charge-transfer resistance, while stabilizing multiple redox-active states. This electronic-structure tuning is consistent with the defect-rich,

strained nanosheet morphology observed from TEM/HRTEM, demonstrating a unified structure–valence–activity mechanism.

Collectively, the mixed-valence cation states, lattice-strain-induced surface defects, and bimetallic electron redistribution establish an active and responsive redox environment. These features create abundant accessible sites and accelerate $OH^-$/$H^+$ intercalation pathways, thereby contributing to the enhanced pseudocapacitive behavior of $NiCo_2Se_4$/CC.

### 3.4. Electrochemical performance and interfacial properties

**3.4.1 Three-electrode performance.** Electrochemical characterization was performed to elucidate how the engineered $NiCo_2Se_4$/CC architecture dictates redox charge storage. As shown in Fig. 5a, the $NiCo_2Se_4$/CC electrode presents an enlarged CV envelope and sharper, more defined redox peaks at 10 mV $s^{-1}$ compared with $NiSe_2$/CC and $CoSe_2$/CC. The higher peak currents, compressed peak-to-peak separation, and near-symmetric anodic/cathodic responses indicate likely accelerated faradaic kinetics and enhanced reversibility. These features signify a shift toward quasi-reversible redox behavior, consistent with an electrode capable of fast ion–electron coupling, as further evidenced by a dominant pseudocapacitive contribution of ~80% for $NiCo_2Se_4$/CC at 10 mV $s^{-1}$ (Fig. S4).

GCD analysis provides a quantitative benchmark of the charge-storage capability of $NiCo_2Se_4$/CC (Fig. 5c). At 1 A $g^{-1}$, the electrode delivers a long discharge time of 680.7 s, longer than $NiSe_2$/CC (54.9 s) and $CoSe_2$/CC (37.8 s, Fig. S2). Even at elevated rates, $NiCo_2Se_4$/CC maintains substantially longer discharge durations—445.9 s (2 A $g^{-1}$), 122.9 s (5 A $g^{-1}$), and 52.9 s (10 A $g^{-1}$)—whereas the monometallic electrodes rapidly collapse to only seconds of output (*e.g.*, 0.5 s for $NiSe_2$/CC at 10 A $g^{-1}$). Correspondingly, $NiCo_2Se_4$/CC delivers a high capacitance of 1479 F $g^{-1}$(4.42 F $cm^{-2}$) at 1 A $g^{-1}$ and retains 90.1% at 10 A $g^{-1}$, whereas $NiSe_2$/CC and $CoSe_2$/CC retain only ~11.5% and ~56.8%, respectively (SI). This high rate capability reflects reduced kinetic polarization and rapid charge propagation within the electrode[52] 4.4. Mechanistically, the vertically aligned nanosheet network maximizes active-site exposure and ensures short ion-diffusion lengths, while intimate coupling with the carbon cloth provides continuous, low-resistance electron pathways. In contrast, the block-like $NiSe_2$ and rod-like $CoSe_2$ structures restrict electrolyte access and suppress high-rate charge storage. The observed GCD characteristics of $NiCo_2Se_4$/CC therefore originate from the cooperative effects of hierarchical nanosheet topology and interfacial electronic integration.

**3.4.2 Electrochemical impedance spectroscopy.** Electrochemical impedance spectroscopy (EIS) was employed to investigate the charge-transfer and ion-transport behavior of the $NiCo_2Se_4$/CC electrode. The Nyquist plot (Fig. 5e) exhibits a small semicircle in the high-to-medium frequency region, followed by an inclined line in the low-frequency region, corresponding to interfacial charge transfer and ion diffusion processes, respectively.[53] The EIS spectrum was quantitatively fitted using an equivalent circuit model consisting of solution resistance ($R_s$), charge-transfer resistance ($R_{ct}$) in parallel with a constant phase element (CPE), and Warburg impedance (W) (Fig. S5). The fitted parameters are summarized in Table S1. The relatively small $R_s$ value reflects good electrical contact between the active material and the conductive carbon cloth substrate. In addition, the presence of Warburg impedance indicates ion diffusion within the porous electrode architecture, consistent with the hierarchical nanosheet structure. Moreover, intrinsic defects identified by HRTEM and XPS further enhance the electron/ion transport pathways.

**3.4.3 Cycling stability.** The $NiCo_2Se_4$/CC electrode retains 84% of its initial capacitance after 5000 cycles at 15 A $g^{-1}$ (Fig. 5f). While post-cycling structural characterization was not performed in this study, gradual capacity decay may be attributed to selenium-vacancy formation, surface oxidation, or partial collapse of the nanosheet structure, consistent with previous reports on $NiCo_2Se_4$ electrodes. The hierarchical nanoflower morphology and intimate contact with the carbon cloth substrate are expected to mitigate rapid structural degradation and help maintain charge-storage capability. These observations indicate that, although performance is retained reasonably well under repeated cycling, further optimization may be required to fully address long-term stability at commercially relevant conditions.

**3.4.4 Performance of the assembled asymmetric supercapacitor device.** To evaluate practical applicability, an asymmetric supercapacitor (ASC) was assembled using $NiCo_2Se_4$/CC as the positive electrode and activated carbon (AC) as the negative electrode, exhibiting stable electrochemical behavior within a voltage window of 0–1.7 V under laboratory testing conditions (Fig. 6b).[54] The CV curves retain a quasi-rectangular shape up to 120 mV $s^{-1}$ (Fig. 6c), while the GCD curves exhibit high symmetry (Fig. 6d), suggesting good reversibility and rapid ion transport. The Ragone plot (Fig. 6e) shows that the ASC delivers an energy density of 30.4 Wh $kg^{-1}$ at 2550 W $kg^{-1}$, outperforming most reported transition metal selenide-based ASCs, such as:$CoSe_2$//AC(18.9 Wh $kg^{-1}$),[55] $Ni_{0.85}Se$-2//AC (18.1 Wh $kg^{-1}$),[56] $NiSe_2$//AC (16.9 Wh $kg^{-1}$),[57] $Ni_3Se_2$-24//AC (11.5 Wh $kg^{-1}$),[58] CoSe//AC(18.6 Wh $kg^{-1}$),[59] $MnSe_2$@$NiCo_2Se_4$//AC(63.2 Wh $kg^{-1}$)[60] or $NiCo_2Se_4$/NC//AC (69.2 Wh $kg^{-1}$).[19] Even at high power densities, the device maintains competitive energy output. Notably, the ASC retains 87.6% of its initial capacitance after 20 000 cycles at 5 A $g^{-1}$ with nearly 98.15% coulombic efficiency (Fig. 6f), likely due to the structural integrity and stable interface of the binder-free $NiCo_2Se_4$/CC electrode.

**3.4.5 Discussion: bridging synthesis simplicity with high performance.** Compared with conventional routes involving tube-furnace selenization or secondary post-selenization treatments under inert atmosphere, the present strategy enables direct selenide formation during the hydrothermal process, thereby eliminating the need for a separate post-selenization step. This reduces the total number of processing steps and avoids high-temperature and inert-atmosphere treatments, leading to lower energy input and improved experimental simplicity.

Our results indicate that a rationally designed one-step hydrothermal strategy enables the simultaneous achievement of relatively high electrochemical performance and synthetic

 

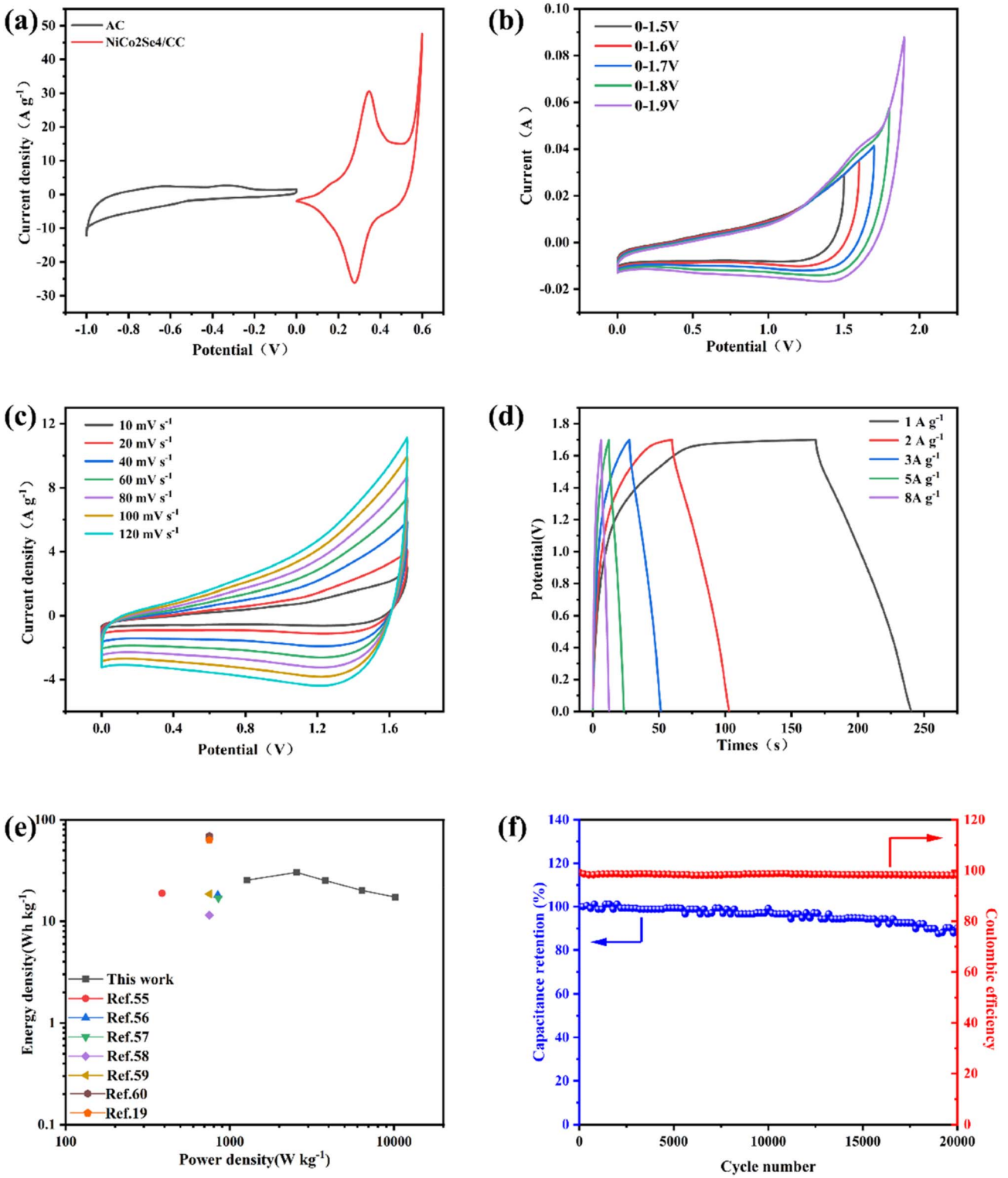


Fig. 6 (a) CV curves at a scan rate of 10 mV $s^{-1}$ for AC and $NiCo_2Se_4$/CC electrodes, (b) CV curves with varied potential ranges for $NiCo_2Se_4$/CC//AC, (c) CV curves at varied scanning rate for $NiCo_2Se_4$/CC//AC, (d) GCD curves at varied current densities for $NiCo_2Se_4$/CC//AC (e) Ragone plot of $NiCo_2Se_4$/CC//AC, (f) cycling performance of $NiCo_2Se_4$/CC//AC at 5 A $g^{-1}$.

simplicity. The properties of $NiCo_2Se_4$/CC can be attributed to its 3D hierarchical nanosheet architecture, mixed Ni/Co valence states, intrinsic structural defects, and intimate binder-free integration with carbon fibers, which together facilitate efficient ion diffusion and moderate charge-transfer resistance. Compared with multistep or defect-engineered methods (Table S3) that often require complex operations, controlled atmospheres, or post-treatments, this one-pot synthesis provides

a straightforward and scalable route to electrodes with competitive performance. These findings illustrate that careful precursor chemistry design can integrally combine structural advantages with electrochemical function in a simple, single-step process.

**3.4.6 Mass loading discussion with experimental support.** It should be noted that the electrochemical performance reported in this work was evaluated at a relatively low mass loading ($3 \pm 0.2$ mg cm$^{-2}$), which is commonly adopted in fundamental studies but may lead to overestimated gravimetric capacitance. To further examine the influence of mass loading, additional electrochemical measurements were conducted at higher loadings of 1, 3, and 5 mg cm$^{-2}$, and the corresponding CV and GCD results are provided in the SI (Fig. S3). As the mass loading increases, the gravimetric capacitance shows a gradual decrease, which can be attributed to limited electrolyte penetration, prolonged ion diffusion pathways, and increased internal resistance in thicker active layers—phenomena widely observed in pseudocapacitive electrodes. In this context, the areal capacitance (4.42 F cm$^{-2}$ at 1 A g$^{-1}$) is reported to better reflect practical charge-storage capability. These results indicate that while the one-step $NiCo_2Se_4$/CC electrode maintains competitive performance at moderate mass loadings, further optimization of electrode thickness and ion-transport pathways will be required to mitigate performance degradation at commercially relevant loadings.

# 4 Conclusion

In summary, a $NiCo_2Se_4$/CC electrode was fabricated *via* a one-step hydrothermal method that emphasizes synthetic simplicity while maintaining good electrochemical performance at a moderate mass loading of ~3 mg cm$^{-2}$. The electrode exhibits a high specific capacitance of 1479 F g$^{-1}$(4.42 F cm$^{-2}$), along with reasonable rate capability, and stable cycling behavior (87.6% retention after 20 000 cycles at 5 A g$^{-1}$). When assembled into an asymmetric supercapacitor with activated carbon, the device delivers an energy density of 30.4 Wh kg$^{-1}$ at 2550 W kg$^{-1}$ while maintaining acceptable cycling performance. This work demonstrates that a streamlined one-step synthesis can produce $NiCo_2Se_4$/CC electrodes with good electrochemical performance without complex post-processing. It should be noted that hydrazine hydrate, used as a reducing agent, is highly toxic. In the current laboratory-scale synthesis, only a small amount (~1–5% v/v of the reaction solution) is required to achieve $NiCo_2Se_4$formation efficiently. While this method is straightforward at the bench scale, industrial-scale implementation would require careful optimization of reagent dosage, use of closed reaction systems, and/or substitution with safer reducing agents. Accordingly, statements regarding scalability and cost-effectiveness have been moderated to reflect these practical considerations. Furthermore, the long-term structural stability of $NiCo_2Se_4$/CC, while reasonably retained in laboratory cycling tests, may be affected by factors such as selenide dissolution or nanosheet degradation under extended or commercial operation.

Overall, this study highlights a rational material design strategy that balances structural characteristics, electrochemical functionality, and synthetic practicality, providing a realistic reference for developing efficient $NiCo_2Se_4$-based electrodes without overstating industrial applicability.

# Conflicts of interest

There is no conflict of interest to declare by all the authors.

# Data availability

The data supporting this article have been included as part of the supplementary information (SI). Supplementary information: Fig. 1–5 and Tables 1–4, detailed experimental procedures, *etc.* See DOI: https://doi.org/10.1039/d6ra00083e.

# Acknowledgements

This work was supported by the National Natural Science Foundation of China (22278255), the Graduate Innovation Fund of Shaanxi University of Science and Technology, and the Shaanxi Provincial Key Research and Development Program Project (2025CY-YBXM-025).

# References

1 B. Tang, Y. Wei, R. Jia, F. Zhang and Y. Tang, *Small*, 2024, **20**, 2308126.
2 G. Smdani, M. R. Islam, A. N. Ahmad Yahaya and S. I. Bin Safie, *Energy Environ.*, 2022, **34**, 1094–1141.
3 F. Wu, M. Liu, Y. Li, X. Feng, K. Zhang, Y. Bai, X. Wang and C. Wu, *Electrochem. Energy Rev.*, 2021, **4**, 382–446.
4 M. S. Khan, M. Shariq, S. M. Bouzgarrou, R. E. Azooz, S. k. Ali, W. A. Ghaly and K. F. Hassan, *Phys. Scr.*, 2024, **99**, 062001.
5 S. Biswas and A. Chowdhury, *ChemPhysChem*, 2023, **24**, e202200567.
6 N. Parvin, D. Merum, M. Kang, S. W. Joo, J. H. Jung and T. K. Mandal, *J. Mater. Chem. A*, 2025, **13**, 24320–24386.
7 A. Pramanik, S. Sengupta, S. K. Saju, S. Chattopadhyay, M. Kundu and P. M. Ajayan, *Adv. Energy Mater.*, 2024, **14**, 2401657.
8 G. Wang, Z. Lu, Y. Li, L. Li, H. Ji, A. Feteira, D. Zhou, D. Wang, S. Zhang and I. M. Reaney, *Chem. Rev.*, 2021, **121**, 6124–6172.
9 H. Wang, N. Deng, S. Wang, X. Wang, Y. Li, Q. Zeng, S. Luo, X. Cui, B. Cheng and W. Kang, *J. Mater. Chem. A*, 2022, **10**, 23433–23466.
10 Z. Wu, *Energy Technol.*, 2024, **12**, 2301574.
11 M. S. Khan, M. Shariq, S. M. Bouzgarrou, R. E. Azooz, S. kashif Ali, W. A. Ghaly and K. Hassan, *Phys. Scr.*, 2024, **99**, 062001.
12 S. Aslam, S. Ahmed and M. Safdar, *J. Electron. Mater.*, 2025, 1–22.
13 M. Madhubalan, S. Sathish, M. Mahivardhan, P. Thandapani, K. K. Abimanyu, R. Kumar, J. H. Seo,

B. W. Gu, S. Muthu Prabhu and B.-h. Jeon, *Small Struct.*, 2025, e202500715.
14 M. M. Ram, R. Sapna, S. R. Rondiya and K. Hareesh, *J. Mater. Chem. A*, 2025, **13**, 40448–40489.
15 M. N. Madni, F. Ahmad, M. Danish, M. Jahangeer, M. U. Islam, M. Adnan, S. Atiq, A. Shakoor and A. Althobaiti, *Solid State Ionics*, 2025, **420**, 116782.
16 L. Liu, Z. Li, W. Peng, J. Chang and H. Wang, *Solid State Ionics*, 2022, **386**, 116046.
17 S. Ghosh, P. Samanta, P. Samanta, N. C. Murmu and T. Kuila, *Energy Fuels*, 2020, **34**, 13056–13066.
18 Z. Guo, Y. Diao, X. Han, Z. Liu, Y. Ni and L. Zhang, *CrystEngComm*, 2021, **23**, 2099–2112.
19 R. Yang, K. T. Alali, X. Guo, K. Song, L. Jia, X. Chen, D. Song, X. Bai and J. Wang, *J. Energy Storage*, 2023, **72**, 108445.
20 B. Jiang, Y. Liu, J. Zhang, Y. Wang, X. Zhang, R. Zhang, L.-L. Huang and D. Zhang, *RSC Adv.*, 2022, **12**, 1471–1478.
21 A. Iqbal, R. Nadeem, A. Shakoor, M. Luqman, M. Mehak, M. U. Salman, S. M. Ramay, F. Ahmad and S. Atiq, *J. Energy Storage*, 2025, **134**, 118207.
22 R. Dallaev, *Polymers*, 2025, **17**, 2346.
23 F. Zou and A. Manthiram, *Adv. Energy Mater.*, 2020, **10**, 2002508.
24 F. Matsumoto and M. Fukunishi, *Batteries*, 2024, **10**, 330.
25 R. E. A. Ardhi, G. Liu, M. X. Tran, C. Hudaya, J. Y. Kim, H. Yu and J. K. Lee, *ACS Nano*, 2018, **12**, 5588–5604.
26 Y. Ding, J. Jiang, Y. Wu, Y. Zhang, J. Zhou, Y. Zhang, Q. Huang and Z. Zheng, *Chem. Rev.*, 2024, **124**, 1535–1648.
27 X. Wu, G. Zhang, X. Zhao, R. Liu, Z. Liu, W. Yang and M. Yang, *Energy Technol.*, 2022, **10**, 2200145.
28 S. Liu, J. Yang, P. Chen, M. Wang, S. He, L. Wang and J. Qiu, *Electrochem. Energy Rev.*, 2024, **7**, 25.
29 A. Shahzad, M. Saleem, A. Shakoor, F. Ahmad, S. Atiq, O. Munir, S. M. B. Arif and N. Bano, *J. Power Sources*, 2025, **656**, 238067.
30 L. Wang, Z. Luo, J. Li, M. Yang, J. Yan, H. Lu, D. Li, C. Chen, M. S. Aghdam and B. Wu, *Postharvest Biol. Technol.*, 2019, **153**, 107–117.
31 A. W. Hashmi, H. S. Mali, A. Meena, K. K. Saxena, S. Ahmad, M. K. Agrawal, B. Sagbas, A. P. V. Puerta and M. I. Khan, *J. Mater. Res. Technol.*, 2023, **23**, 4866–4908.
32 M. Barath Kumar and M. Manikandan, *Met. Mater. Int.*, 2022, **28**, 54–111.
33 Y.-Y. Deng, X.-L. Shi, T. Wu, Y. Yue, W.-D. Liu, M. Li, F. Yue, P. Huang, Q. Liu and Z.-G. Chen, *Adv. Fiber Mater.*, 2024, **6**, 1616–1628.
34 X. Fu, Y. Zhou, J. Huang, L. Feng, P. Yu, Q. Zhang, W. Yang and Y. Wang, *Adv. Energy Mater.*, 2023, **13**, 2301385.
35 R. Zhang and T. Sun, *Heliyon*, 2024, **10**, e33023.
36 W. Dou, M. Zheng, W. Zhang, T. Liu, F. Wang, G. Wan, Y. Liu and X. Tao, *Adv. Funct. Mater.*, 2023, **33**, 2305161.
37 Y. Wang, X. Yuan, K. Ni, Y. Song, X. Li, X. Zeng, B. Shao and B. Sun, *Energy Environ. Sci.*, 2024, **17**, 4780–4793.
38 T. Papalas, E. Palamas, A. N. Antzaras and A. A. Lemonidou, *Fuel*, 2024, **359**, 130272.
39 L. Liu, Z. Wang, J. Zhang, O. Ruzimuradov, K. Dai and J. Low, *Adv. Mater.*, 2023, **35**, 2300643.
40 K. P. Kumar, N. K. Arkoti, N. Chundi, G. Elsa, M. Vijayakumar, M. Karthik and S. Sakthivel, *Chem. Eng. J.*, 2025, **513**, 162859.
41 N. Parvin, D. Merum, M. Kang, S. W. Joo, J. H. Jung and T. K. Mandal, *J. Mater. Chem. A*, 2025, 24320–24386.
42 B. Ramulu, J. A. Shaik, A. R. Mule and J. S. Yu, *Mater. Sci. Eng. R Rep.*, 2024, **160**, 100820.
43 J. Ahn, H. Lim, J. Ko and J. Cho, *Energy Adv.*, 2024, **3**, 2152–2174.
44 R. Manikandan, C. J. Raj, S. E. Moulton, T. S. Todorov, K. H. Yu and B. C. Kim, *Chem. Eur J.*, 2021, **27**, 669–682.
45 H. S. AlSalem, K. M. S. Katubi, M. S. Binkadem, S. T. Al-Goul and A. M. Wahba, *ACS Omega*, 2023, **8**, 40808–40816.
46 Y.-S. Lee, A. R. Selvaraj, N. Kostoglou, C. Rebholz, R. Rajendiran, V. Raman, H. Kim, J. A. Rajesh, V. M. Nagulapati and T. H. Oh, *Mater. Sci. Eng. B*, 2024, **304**, 117368.
47 S. Peng, S. Lu, X. Wang, L. Dai, B. Chen, Y. Wu, Q. Xie and Y. Ruan, *Colloids Surf. A Physicochem. Eng. Asp.*, 2024, **688**, 133666.
48 M. Li, F. Sun, F. Hong and B. Shan, *ChemCatChem*, 2025, e01256.
49 T. Ramachandran, R. K. Raji and I. Hussain, *Sustain. Energy Fuels*, 2025, **9**, 6116–6149.
50 A. Güngör, A. U. Ammar, A. M. Rostas and E. Erdem, *J. Mater. Chem. A*, 2025, **13**, 36030–36055.
51 X. Liu, Y. Bao, L. Yuan, H. Zhao, W. Tian and J. Ji, *J. Mater. Chem. A*, 2025, **13**, 35024–35053.
52 R. E. A. Ardhi, G. Liu and J. K. Lee, *ACS Energy Lett.*, 2021, **6**, 1432–1442.
53 F. Meng, J. McKechnie, T. Turner, K. H. Wong and S. J. Pickering, *Environ. Sci. Technol.*, 2017, **51**, 12727–12736.
54 G. Yang, M. L. Lehmann, S. Zhao, B. Li, S. Ge, P.-F. Cao, F. M. Delnick, A. P. Sokolov, T. Saito and J. Nanda, *Energy Storage Mater.*, 2021, **35**, 431–442.
55 S. Liu, S. Sarwar, J. Wang, H. Zhang, T. Li, J. Luo and X. Zhang, *J. Mater. Chem. C*, 2021, **9**, 228–237.
56 B. Ma, M. Peng, S. Zhang, Q. Zhou, L. Wang, Y. Zhang, Q. Luo, J. An, H. Mu, H. Zhang, Z. Li, X. Yin, Y. Duan and D. Wang, *Appl. Catal. B Environ. Energy*, 2025, **364**, 124857.
57 Y. Gu, W. Du, Y. Darrat, M. Saleh, Y. Huang, Z. Zhang and S. Wei, *Appl. Nanosci.*, 2020, **10**, 1591–1601.
58 Y. Ma, H. Du, S. Zheng, Z. Zhou, H. Zhang, Y. Ma, S. Passerini and Y. Wu, *Energy Storage Mater.*, 2025, **79**, 104295.
59 H. Chen, J. Li, L. Xiang, K. Liu, Y. Pan, X. Li, J. Chen, D. Lin, X. Li, S. Zhang, C. Xing and P. Xue, *Chem. Eng. J.*, 2025, **523**, 168397.
60 X. Sun, K. Zhao, H. Fu, H. Guo, J. Shen, F. Jin, L. Wang, Z. Wang, L. Cui, F. Quan and J. Liu, *J. Energy Storage*, 2023, **63**, 107041.